

Next-to-leading order QCD corrections to five jet production at the LHCSimon Badger^{*}*The Niels Bohr Institute, Niels Bohr International Academy and Discovery Center,
University of Copenhagen, Blegdamsvej 17, DK-2100 Copenhagen, Denmark*Benedikt Biedermann[†]*Institut für Physik, Humboldt-Universität zu Berlin, Newtonstraße 15, D-12489 Berlin, Germany*Peter Uwer[‡]*Institut für Physik, Humboldt-Universität zu Berlin, Newtonstraße 15, D-12489 Berlin, Germany*Valery Yundin[§]*The Niels Bohr Institute, Niels Bohr International Academy and Discovery Center,
University of Copenhagen, Blegdamsvej 17, DK-2100 Copenhagen, Denmark*

(Received 8 October 2013; published 19 February 2014)

We present theoretical predictions for five-jet production in proton-proton collisions at next-to-leading-order accuracy in QCD. Inclusive as well as differential observables are studied for collision energies of 7 and 8 TeV. In general the next-to-leading-order corrections stabilize the theoretical predictions with respect to scale variations. In the case of the inclusive jet cross sections, we compare with experimental data where possible and find reasonable agreement. We observe that the four-to-three and five-to-four jet ratios show better perturbative convergence than the known three-to-two ratio and are promising candidates for future α_s measurements. Furthermore, we present a detailed analysis of uncertainties related to parton distribution functions. The full color virtual matrix elements used in the computation were obtained with the NJET package [1], a publicly available library for the evaluation of one-loop amplitudes in massless QCD.

DOI: 10.1103/PhysRevD.89.034019

PACS numbers: 12.38.Bx, 14.65.Ha

I. INTRODUCTION

The wealth of data recorded at the LHC experiments in run 1 presents an excellent opportunity to test QCD in a new energy regime. Furthermore, multijet production at large transverse momentum can provide useful information to constrain the parton distribution functions (PDFs). Where precise theoretical results are available, the data can also be used to determine the strong coupling constant α_s . In that context large multiplicities may turn out to be particularly useful, in analogy to what has been observed in electron-positron annihilation. Pure QCD reactions with multiple jet production can also give large backgrounds to various new physics searches, and therefore precision predictions are required.

Next-to-leading-order (NLO) predictions at fixed order in α_s for dijet production have been known for more than 20 years [2]. Three-jet production represents a considerable increase in computational complexity, and a full computation was completed in 2002 [3] and implemented in the public code NLOJET++, though pure gluonic contributions were

known previously [4]. Breakthroughs in virtual amplitude computations have recently enabled predictions of four-jet production [5,6], with results generally in good agreement with the experimental data [7]. Dijet production is known to suffer from large corrections from soft gluon radiation which requires resummation beyond fixed-order perturbation theory. Theoretical predictions at NLO including the parton shower (NLO + PS) allow one to account for these effects and obtain a better description of the available data [8,9]. The CMS Collaboration has recently completed a measurement of α_s from the inclusive three-jet to inclusive two-jet ratio. The measurement illustrates well the LHC's potential for precision measurements. With next-to-next-to-leading-order QCD corrections to dijet production just around the corner [10], theoretical uncertainties look to be under good control and enable future QCD predictions to move beyond the “industry standard” LO + PS/ME (*matrix element*) + PS accuracy.

There has been much progress in the automation of NLO computations. Processes with four or five final-state particles—previously thought to be impossible—are now available in public codes [1,11–14]. New methods and algorithms [15–18] have been pushing the boundaries of perturbative QCD computations and increasing the range of phenomenological applications (recent examples can be found in Refs. [19–23]; see also Ref. [24] for a more complete overview). Powerful on-shell unitarity methods

^{*}badger@nbi.dk[†]benedikt.biedermann@physik.hu-berlin.de[‡]peter.uwer@physik.hu-berlin.de[§]yundin@nbi.dk

have been available for many years [25,26] which continue to demonstrate the ability to simplify calculations of extremely high multiplicity amplitudes that are inaccessible with alternative tools. Recent state-of-the-art computations include the NLO QCD corrections to $pp \rightarrow W + 5$ jets [20] by the BLACKHAT Collaboration. In this paper we present the first computation for the production of five hard jets at NLO in QCD. High-multiplicity computations such as this one would be interesting to compare with predictions of universal scaling patterns for QCD jets [27], though six-jet production would be the first occasion where it would be possible to extract a statistical error on such a fit from a fixed-order computation.

This article is organized as follows. We first give an overview of the computational framework for the various partonic subchannels in Sec. II. Section III contains our results for the NLO QCD corrections to $pp \rightarrow 5$ jets. We describe the numerical setup and interface with the SHERPA Monte Carlo (MC) event generator [28] in Sec. III A along with kinematic cuts. Results for total cross sections and jet ratios are compared to the available data in Sec. III B. We present differential distributions in the jet transverse momenta and rapidity and perform a detailed comparison of different PDF fits. We finally present our conclusions and outlook for the future. Two appendices containing a complete set of distributions and numerical values used in the plotted histograms are included to ease future comparisons.

II. OUTLINE OF THE CALCULATION

The calculation is done in QCD with five massless quark flavors including the bottom quark in the initial state. We expect the neglected contributions from top-quark loops to be much smaller than the estimated theoretical uncertainty.¹ The processes contributing to five-jet production may be derived from the following four basic channels via crossing symmetry:

$$\begin{aligned} 0 &\rightarrow gggggg, & 0 &\rightarrow q\bar{q}ggggg, \\ 0 &\rightarrow q\bar{q}q'\bar{q}'ggg, & 0 &\rightarrow q\bar{q}q'\bar{q}'q''\bar{q}''g, \end{aligned}$$

where q , q' , and q'' denote generic quarks of different flavor. Amplitudes with like-flavor quark pairs can always be obtained from the amplitudes for different flavors by an appropriate (anti)symmetrization. The n -jet differential cross section expanded in the coupling α_s reads

$$d\sigma_n = d\sigma_n^{\text{LO}} + d\delta\sigma_n^{\text{NLO}} + \mathcal{O}(\alpha_s^{n+2}), \quad (1)$$

¹Through the matching between five- and six-flavor QCD, logarithmically enhanced terms of ultraviolet origin are taken into account. Power-suppressed terms are however neglected. Since the massless quark loops contribute less than 5% to the total cross section for $N_f = 5$ we expect the contribution from closed top-quark loops to the total cross section to be very small. At large transverse momenta the effect of power-suppressed terms may however increase.

where $d\sigma_n^{\text{LO}} \sim \alpha_s^n$ and $d\delta\sigma_n^{\text{NLO}} \sim \alpha_s^{n+1}$. In the QCD-improved parton model, the leading-order differential cross section $d\sigma_n^{\text{LO}}$ is given by

$$\begin{aligned} d\sigma_n^{\text{LO}} &= \sum_{i,j \in \{q,\bar{q},g\}} dx_i dx_j F_{j/H_2}(x_j, \mu_f) F_{i/H_1}(x_i, \mu_f) \\ &\times d\sigma_n^{\text{B}}(i(x_i P_1) + j(x_j P_2) \rightarrow n \text{ part.}). \end{aligned} \quad (2)$$

P_1, P_2 are the momenta of the two incoming hadrons H_1, H_2 , which we assume to be massless. The total incoming momentum of the initial-state partons $P = x_i P_1 + x_j P_2$ leads to a partonic center-of-mass energy squared $\hat{s} = 2x_i x_j (P_1 \cdot P_2) = x_1 x_2 s_{\text{had}}$, with s_{had} being the hadronic center-of-mass energy squared. The parton distribution functions $F_{i/H}(x, \mu_f)$ describe, roughly speaking, the probability to find a parton i inside a hadron H with a momentum fraction between x and $x + dx$. Note that, in addition to x , the parton distribution functions also depend on the unphysical factorization scale μ_f . The partonic differential cross section $d\sigma_n^{\text{B}}(i(x_i P_1) + j(x_j P_2) \rightarrow n \text{ part.})$ describes the reaction ($ij \rightarrow n$ -jets) in the Born approximation using the leading-order matrix elements $|\mathcal{M}_n(ij \rightarrow n \text{ part.})|^2$ and a suitable jet algorithm $\Theta_{n\text{-jet}}$,

$$\begin{aligned} d\sigma_n^{\text{B}} &= \frac{1}{2\hat{s}} \prod_{\ell=1}^n \frac{d^3 k_\ell}{(2\pi)^3 2E_\ell} \Theta_{n\text{-jet}} \\ &\times (2\pi)^4 \delta\left(P - \sum_{m=1}^n k_m\right) |\mathcal{M}_n(ij \rightarrow n \text{ part.})|^2. \end{aligned} \quad (3)$$

k_i are the four-momenta of the outgoing partons obeying $\hat{s} = (\sum_{i=1}^n k_i)^2$. The jet algorithm $\Theta_{n\text{-jet}}$ is a function depending solely on the final-state parton momenta k_i and on parameters defining the geometric extensions of the jet. Its value is equal to 1 if the final-state momentum configuration corresponds to a valid n -jet event, and it is 0 otherwise. The Born matrix elements $\mathcal{M}(ij \rightarrow n \text{ part.})$ have been evaluated with COMIX [29] within the SHERPA framework. The SHERPA Monte Carlo event generator [30] has also been used to perform the numerical phase-space integration.

At NLO accuracy both the virtual corrections $d\sigma_n^{\text{V}}$ (one-loop contribution interfered with the Born amplitude) and the real corrections $d\sigma_{n+1}^{\text{R}}$ (tree-level amplitudes with one additional parton in the final state) contribute to the n -jet cross section. Both $d\sigma_n^{\text{V}}$ and $d\sigma_{n+1}^{\text{R}}$ contain separately collinear and soft divergences. Only after combining the two contributions and factorizing the initial-state singularities into renormalized parton distributions does one obtain a finite result. In order to perform the cancellation of the divergences numerically we apply the Catani-Seymour subtraction method [31]. The idea is to add and subtract local counterterms $d\sigma_{n+1}^{\text{S}}$ with $(n+1)$ -parton kinematics which, on the one hand, mimic pointwise the singularity structure of the real corrections and, on the other hand, are chosen such that the singularity due to the additional parton emission can be calculated analytically via

separate integration of the one-particle phase space. Since by construction the latter cancel the divergences from the virtual corrections, only finite quantities remain, making the numerical integration with a Monte Carlo program feasible. Schematically, we may write the total cross section as

$$\delta\sigma^{\text{NLO}} = \int_n \left(d\sigma_n^{\text{V}} + \int_1 d\sigma_{n+1}^{\text{S}} \right) + \int_n d\sigma_n^{\text{Fac}} + \int_{n+1} (d\sigma_{n+1}^{\text{R}} - d\sigma_{n+1}^{\text{S}}). \quad (4)$$

$d\sigma_n^{\text{Fac}}$ is due to the factorization of initial-state singularities. The NLO corrections can then be written in terms of three finite contributions,

$$d\delta\sigma_n^{\text{NLO}} = d\bar{\sigma}_n^{\text{V}} + d\bar{\sigma}_n^{\text{I}} + d\sigma_{n+1}^{\text{RS}}, \quad (5)$$

where $d\bar{\sigma}_n^{\text{V}}$ denotes the finite part of the virtual corrections, $d\bar{\sigma}_n^{\text{I}}$ the finite part of the integrated subtraction terms together with the contribution from the factorization, and $d\sigma_{n+1}^{\text{RS}}$ the real corrections combined with the subtraction terms. For the computation of $d\bar{\sigma}_n^{\text{I}}$ and $d\sigma_{n+1}^{\text{RS}}$ we use SHERPA, which provides a numerical implementation of the Catani-Seymour subtraction scheme. The required tree-level amplitudes are, as in the LO case, computed with COMIX as part of the SHERPA framework.

The necessary one-loop matrix elements for the virtual corrections $d\bar{\sigma}_n^{\text{V}}$ are evaluated with the publicly available NJET² package [1]. NJET uses an on-shell generalized unitarity framework [32–35] to compute multiparton one-loop primitive amplitudes from tree-level building blocks. An accurate numerical implementation is achieved using the integrand reduction procedure of Ossola, Papadopoulos, and Pittau [36]. For a more complete discussion of these methods we refer the reader to a recent review in Ref. [37] and references therein. The algorithm is based on the NGLUON library [11], following the description of D -dimensional generalized unitarity presented in Refs. [38,39] and using Berends-Giele recursion [40] for efficient numerical evaluation of tree-level amplitudes. For a more detailed description of the employed methods and the usage of the program, we refer to Refs. [1,11]. The scalar loop integrals are obtained via the QCDLOOP/FF package [41,42]. We note that NJET is so far the only publicly available tool that is able to compute all one-loop seven-point matrix elements that contribute to five-jet production in hadronic collisions. For reference, numerical evaluations of the one-loop matrix elements at a single phase-space point have been presented previously [1].

²To download NJET visit the project home page at <https://bitbucket.org/njet/njet/>.

III. RESULTS FOR FIVE-JET PRODUCTION AT THE LHC AT 7 AND 8 TeV

A. Numerical setup

As mentioned earlier, we use the SHERPA Monte Carlo event generator [28] to handle phase-space integration and the generation of tree-level and Catani-Seymour dipole subtraction terms using the color-dressed formalism implemented in COMIX [29,30]. The virtual matrix elements are interfaced using the Binot Les Houches Accord [43,44].

To combine partons into jets we use the anti- k_t jet clustering algorithm as implemented in FASTJET [45,46]. Furthermore asymmetric cuts on the jets ordered in transverse momenta, p_T , are applied to match the ATLAS multijet measurements [7],

$$p_T^{j_1} > 80 \text{ GeV}, \quad p_T^{j_{\geq 2}} > 60 \text{ GeV}, \quad R = 0.4. \quad (6)$$

The PDFs are accessed through the LHAPDF interface [47], with all central values using NNPDF2.1 [48] for LO [$\alpha_s(M_Z) = 0.119$] and NNPDF2.3 [49] for NLO [$\alpha_s(M_Z) = 0.118$] if not mentioned otherwise.

Generated events are stored in Root Ntuple format [50] which allows for flexible analysis. Renormalization and factorization dependence can be reweighted at the analysis level, as well as the choice of PDF set. Since the event generation of high-multiplicity processes at NLO is computationally intensive, an analysis of PDF uncertainties and scale choices would be prohibitive without this technique. We note that the Root Ntuple files can also be used to provide NLO results directly to the experimental collaborations.

B. Numerical results

In this section we present the numerical results for total cross sections and selected³ distributions at center-of-mass energies of 7 and 8 TeV. Within the setup described in the previous section we have chosen the renormalization and factorization scales to be equal, $\mu_r = \mu_f = \mu$, and we use a dynamical scale based on the total transverse momentum \hat{H}_T of the final-state partons,

$$\hat{H}_T = \sum_{i=1}^{N_{\text{parton}}} p_{T,i}^{\text{parton}}. \quad (7)$$

We then obtain the five-jet cross section at 7 TeV:

μ	$\sigma_5^{7 \text{ TeV-LO}}$ [nb]	$\sigma_5^{7 \text{ TeV-NLO}}$ [nb]
$\hat{H}_T/2$	0.699(0.004)	0.544(0.016)
\hat{H}_T	0.419(0.002)	0.479(0.008)
$\hat{H}_T/4$	1.228(0.006)	0.367(0.032)

³The complete set of results presented in this section together with additional distributions for 7 and 8 TeV can be obtained from <https://bitbucket.org/njet/njet/wiki/Results/Physics>.

(Numerical integration errors are quoted in parentheses.) We show the values of the cross section at three values of the renormalization scale, $\mu = x\hat{H}_T/2$, where $x = 0.5, 1, 2$. We observe significant reduction in the residual scale dependence when including NLO corrections. Within the chosen scale band, the LO predictions lie within a range of 0.810 nb, while at NLO the range is 0.177 nb. The analogous results at 8 TeV are shown below.

μ	$\sigma_3^8 \text{ TeV-LO [nb]}$	$\sigma_3^8 \text{ TeV-NLO [nb]}$
$\hat{H}_T/2$	1.044(0.006)	0.790(0.021)
\hat{H}_T	0.631(0.004)	0.723(0.011)
$\hat{H}_T/4$	1.814(0.010)	0.477(0.042)

In Fig. 1 the scale dependence of the leading-order and next-to-leading-order cross section is illustrated. The dashed black line indicates $\mu = \hat{H}_T/2$. The horizontal bands show the variation of the cross section for a scale variation between $\hat{H}_T/4$ and \hat{H}_T . The uncertainty due to scale variation is roughly reduced by a factor of one third. Furthermore, we see that around $\mu = \hat{H}_T/2$ the NLO cross section is flat, indicating that $\mu = \hat{H}_T/2$ is a reasonable choice for the central scale. This is further supported by the fact that for $\mu = \hat{H}_T/2$ the NLO corrections are very small. It is also interesting to observe that the two bands, LO and NLO, nicely overlap. Note however that we have used the NLO setup in the leading-order calculation. In particular, the NLO PDFs with the corresponding α_s are employed. In Fig. 2 we show the scale dependence using LO PDFs in the leading-order prediction with the respective α_s . Compared to Fig. 1, we observe in Fig. 2 a much larger difference between the LO and NLO predictions. To some extent the difference is due to the change in α_s . Similar to what was found in Ref. [6], we conclude that using the NLO PDFs in the LO predictions gives a better approximation to the full result compared to using LO PDFs.

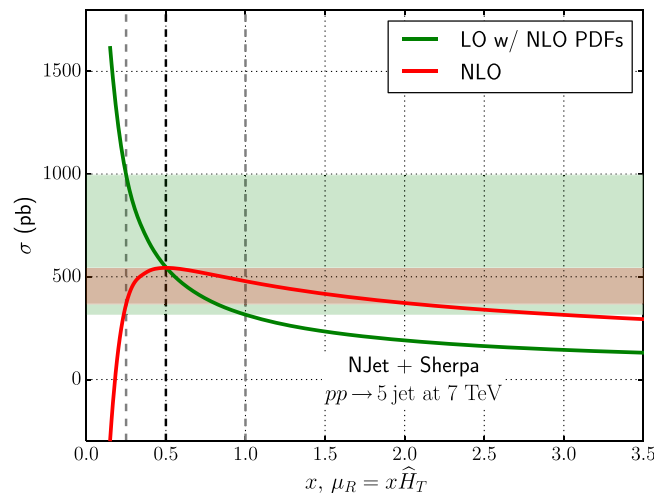


FIG. 1 (color online). Same as Fig. 2 but using the NLO setup in LO.

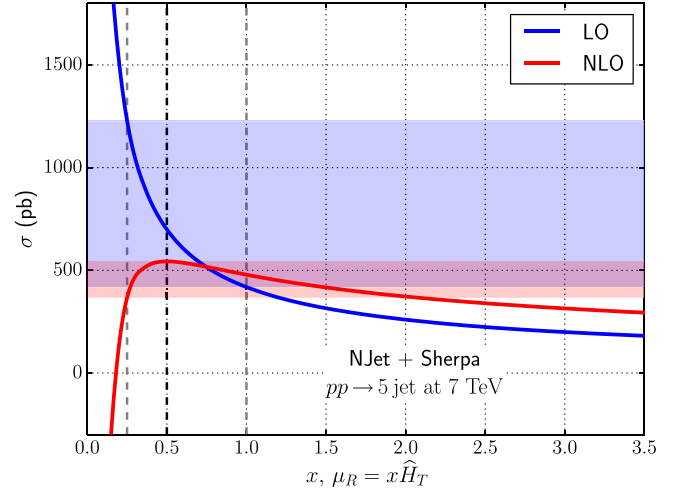


FIG. 2 (color online). Residual scale dependence of the five-jet cross section in leading and next-to-leading order.

Although not a physical observable, it is interesting to ask how the different partonic channels contribute to the inclusive five-jet rate. Ignoring different quark flavors, we distinguish nine partonic channels in LO,

$$\begin{aligned}
 gg &\rightarrow 5g, & gg &\rightarrow qq + 3g, & qq &\rightarrow q + 4g, \\
 qq &\rightarrow 5g, & gg &\rightarrow 4q + g, & qq &\rightarrow 3q + 2g, \\
 qq &\rightarrow qq + 3g, & qq &\rightarrow 5q, & qq &\rightarrow 4q + g,
 \end{aligned}$$

where q may be any quark or antiquark with the exception of the top quark, i.e., $qq = \{uu, u\bar{u}, ud, u\bar{d}, \dots\}$. In Table I the individual contribution of each channel is presented. The most important contribution is provided by the qq initial state. Almost 50% of the cross section can be attributed to this channel. This is a consequence of the large parton luminosity in combination with the sizeable cross sections. Among the qq -initiated reactions the $qq \rightarrow q + 4g$ channel is the most important process, accounting for about 40% of the cross section. Replacing the quark line in this process by a gluon will still lead to large partonic cross sections. However, the gg parton flux is reduced compared to the qq initial state. As a consequence

TABLE I. Contribution of individual partonic channels.

$qq \rightarrow q + 4g$	39.2%
$gg \rightarrow 5g$	27.3%
$qq \rightarrow 2q + 3g$	13.5%
$qq \rightarrow 3q + 2g$	9.0%
$gg \rightarrow 2q + 3g$	8.5%
$qq \rightarrow 4q + g$	1.8%
$gg \rightarrow 4q + g$	0.5%
$qq \rightarrow 5q$	0.2%
$qq \rightarrow 5g$	0.04%

the purely gluonic reaction leads to a slightly smaller contribution and is responsible for about 25% of the cross section. The composition of the cross section may provide useful information when jet rates are used to constrain the PDFs. Since the luminosity functions

$$\mathcal{L}_{ij}(\hat{s}, s_{\text{had}}, \mu_f) = \frac{1}{s_{\text{had}}} \int_{\hat{s}}^{s_{\text{had}}} \frac{ds}{s} F_{i/p}\left(\mu_f, \frac{s}{s_{\text{had}}}\right) F_{j/p}\left(\mu_f, \frac{\hat{s}}{s}\right) \quad (8)$$

depend on the partonic center-of-mass energy, the composition may be different for different kinematical configurations. We will come back to this point when we discuss differential distributions.

In Table II we show for completeness the cross sections for two-, three-, and four-jet production as calculated with NJET using the same setup as in the five-jet case. The real corrections to five-jet production also allow us to calculate the cross section for six-jet production, albeit only in leading-order QCD. The results are as follows:

μ	$\sigma_6^{7 \text{ TeV-LO}}$ [nb]	$\sigma_6^{8 \text{ TeV-LO}}$ [nb]
$\hat{H}_T/2$	0.0496(0.0005)	0.0844(0.0010)
\hat{H}_T	0.0263(0.0003)	0.0452(0.0005)
$\hat{H}_T/4$	0.0992(0.0011)	0.1673(0.0021)

Here the NNPDF2.3 NLO PDF set with $\alpha_s = 0.118$ has been used. The jet rates have been measured recently by ATLAS using the 7 TeV data set [7]. In Fig. 3 we show the data together with the theoretical predictions in leading and next-to-leading order. In the case of the six-jet rate only LO results are shown. In the lower plot the ratio of theoretical predictions with respect to data is given. With the exception of the two-jet cross section, the inclusion of the NLO results significantly improves the comparison with data. For the higher multiplicities where NLO predictions are available the ratio between theory and data is about 1.2–1.3. Given that inclusive cross sections are intrinsically difficult to measure, we consider this agreement as remarkably good. In particular, for three-, four-, and five-jet production the theoretical predictions agree within the uncertainties with the data. One should also keep in mind that a one percent uncertainty of the collider energy may lead to sizeable changes in the cross sections. [For example, the

TABLE II. Results for two-, three-, and four-jet production with the same setup as in the five-jet case. All values are in units of nb.

μ	$\sigma_2^{7 \text{ TeV-NLO}}$ [nb]	$\sigma_3^{7 \text{ TeV-NLO}}$ [nb]	$\sigma_4^{7 \text{ TeV-NLO}}$ [nb]
$\hat{H}_T/2$	1175(3)	52.5(0.3)	5.65(0.07)
\hat{H}_T	1046(2)	54.4(0.2)	5.36(0.04)
$\hat{H}_T/4$	1295(4)	33.2(0.4)	3.72(0.12)

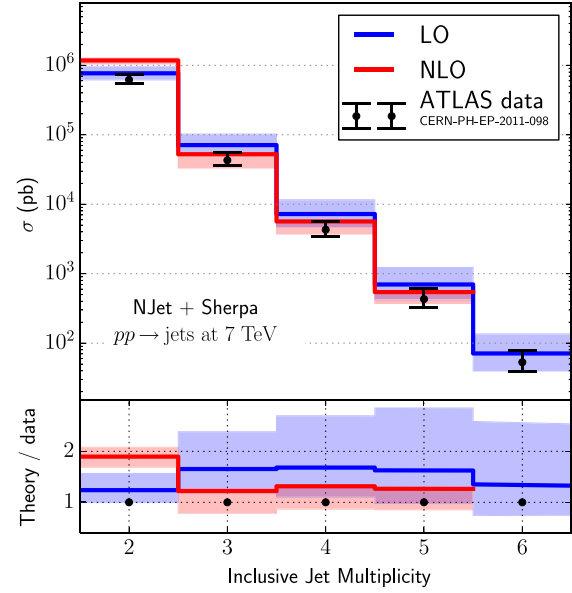


FIG. 3 (color online). Cross sections for two-, three-, four-, five- and six-jet production in leading and next-to-leading order as calculated with NJET, as well as results from ATLAS measurements [7]. All LO quantities use NNPDF2.1 with $\alpha_s(M_Z) = 0.119$. NLO quantities use NNPDF2.3 with $\alpha_s(M_Z) = 0.118$; the six-jet cross section is only available at LO accuracy.

inclusive cross section for top-quark pair production changes by about 3% when the energy is changed from 7 TeV to (7 ± 0.07) TeV.] Instead of studying inclusive cross sections it is useful to consider their ratios, as many theoretical and experimental uncertainties (i.e., uncertainties due to luminosity, scale dependence, PDF dependence, etc.) may cancel between numerator and denominator. In particular, one may consider

$$\mathcal{R}_n = \frac{\sigma_{(n+1)\text{-jet}}}{\sigma_{n\text{-jet}}}. \quad (9)$$

This quantity is proportional to the QCD coupling α_s in leading order and can be used to determine the value of α_s from jet rates. In Fig. 4 we show QCD predictions in NLO using different PDF sets together with the results from ATLAS. The results obtained from NNPDF2.3 are also collected in Table III where, in addition, the ratios at leading order (using the LO setup with NNPDF2.1) are shown. In the case of \mathcal{R}_3 and \mathcal{R}_4 , perturbation theory seems to provide stable results. The leading-order and next-to-leading-order values differ by less than 10%. In addition, NNPDF [49], CT10 [51], and MSTW08 [52] give compatible predictions. ABM11 [53] gives slightly smaller results for \mathcal{R}_3 and \mathcal{R}_4 . Within uncertainties the predictions also agree with the ATLAS measurements. For \mathcal{R}_2 a different picture is observed. First of all, the theoretical

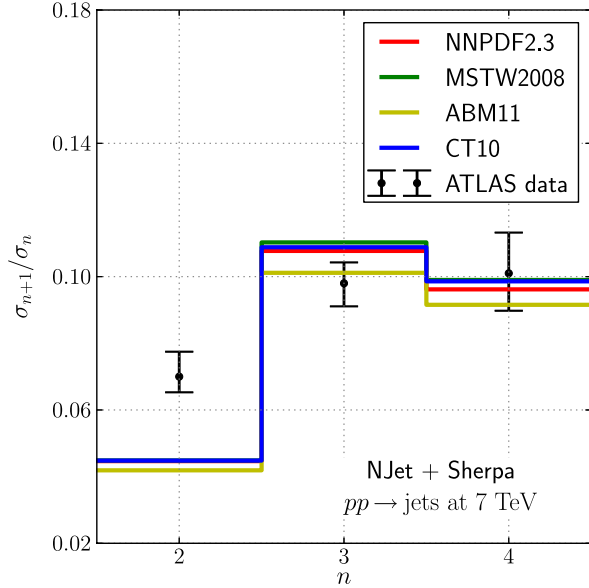


FIG. 4 (color online). Theoretical predictions for the jet ratios \mathcal{R}_n compared with recent ATLAS measurements [7]. Theoretical predictions are made with the central values of the four listed PDF sets with NLO α_s running. $\alpha_s(m_Z) = 0.118$ for NNPDF2.3, CT10, and ABM11, and $\alpha_s(m_Z) = 0.120$ for MSTW2008

predictions change by about -50% when going from LO to NLO. The origin of this behavior is traced back to the inclusive two-jet cross section which is affected by large perturbative corrections. As a function of the leading jet p_T , all PDF sets agree well with the $3/2$ ratio from the ATLAS data at large p_T , as shown in Fig. 5. In Fig. 6 we compare LO and NLO predictions for \mathcal{R}_n as a function of the leading jet p_T . While for \mathcal{R}_3 and \mathcal{R}_4 the corrections are moderate, for all values of p_T we observe large negative corrections independent from p_T in the case of \mathcal{R}_2 . Most likely the two-jet rate is very sensitive to soft gluon emission while the higher jet multiplicities are less affected. As a consequence the fixed-order calculations fail to give reliable predictions for the two-jet rate. A possible improvement could be expected from soft gluon resummation and matching with parton shower calculations. As long as only fixed-order calculations are used to predict \mathcal{R}_2 we do not expect a perfect agreement with the data, especially in the low- p_T region. Similar to what is observed in Fig. 3,

TABLE III. Results for the jet ratios \mathcal{R}_n for the central scale of $\hat{H}_T/2$ and the NNPDF2.3 PDF set.

\mathcal{R}_n	ATLAS [7]	LO	NLO
2	$0.070^{+0.007}_{-0.005}$	0.0925(0.0002)	0.0447(0.0003)
3	$0.098^{+0.006}_{-0.007}$	0.102(0.000)	0.108(0.002)
4	$0.101^{+0.012}_{-0.011}$	0.097(0.001)	0.096(0.003)
5	$0.123^{+0.028}_{-0.027}$	0.102(0.001)	...

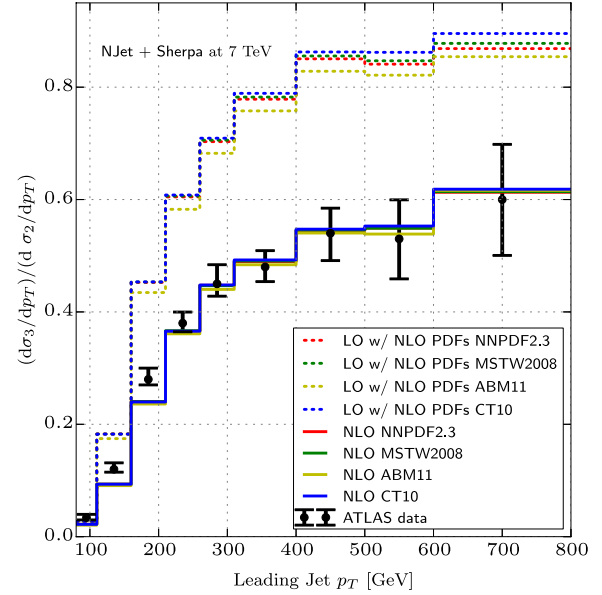


FIG. 5 (color online). The $3/2$ jet ratio as a function of the p_T of the leading jet. ATLAS data is taken from Ref. [7]. The cuts are given in Sec. III A except the jet-cone radius, which is taken as $R = 0.6$.

the comparison with data indeed shows significant discrepancy in \mathcal{R}_2

Let us now move on to less inclusive quantities. In Fig. 7 we show the transverse momentum distribution of the leading jet for five-jet production. Similar to the inclusive quantities, a significant reduction of the scale uncertainty is observed when going from LO to NLO. Using again the

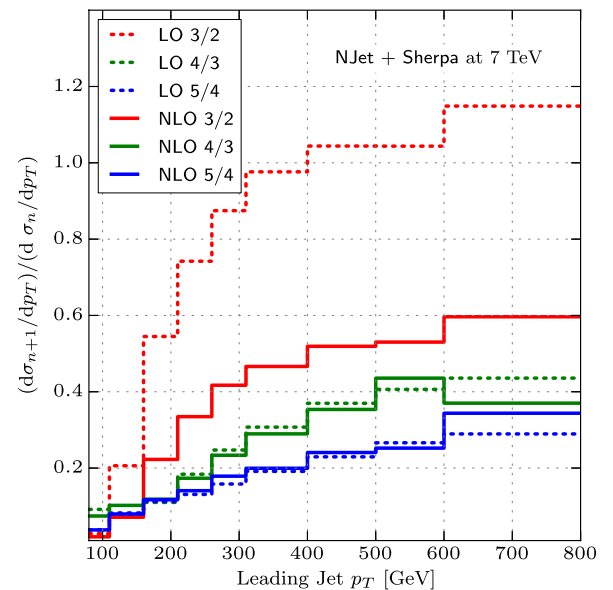


FIG. 6 (color online). The \mathcal{R}_n ratio as a function of the p_T of the leading jet.

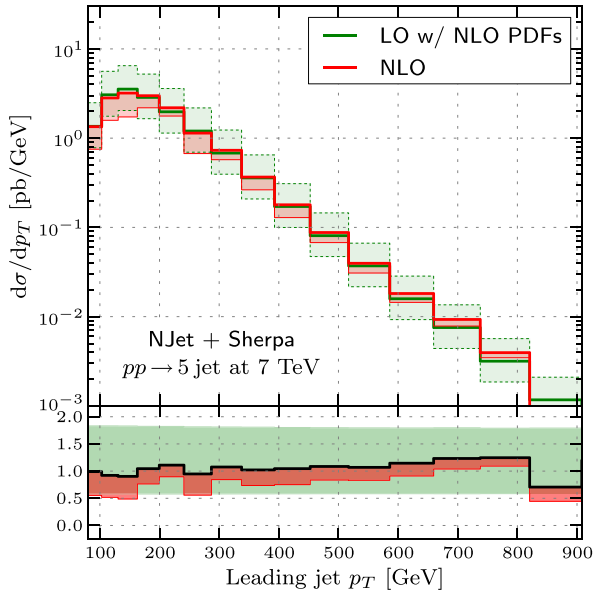


FIG. 7 (color online). The p_T distribution of the leading jet. Both LO and NLO use the NNPDF2.3 PDF set with $\alpha_s(M_Z) = 0.118$.

NLO setup to calculate the LO predictions, the NLO calculation gives very small corrections. Over a wide range the LO predictions are modified by less than 10%. A remarkable feature observed already in the four-jet calculation [5,6] is the almost constant K factor. Again, the dynamical scale seems to resum possible large logarithms which would appear at large transverse momentum using a

fixed scale. Similar findings apply to the transverse momentum distribution of the subleading jets. In Fig. 8 we show the rapidity distribution of the leading jet, again in LO and NLO QCD. In the range $-2 < \eta < 2$ the distribution is remarkably flat. Again, the NLO corrections are below 10% for most η values and the K factor is roughly constant. We have also investigated differential distributions for a center-of-mass energy of 8 TeV. Studying normalized distributions to account for the increase of the inclusive jet cross section when going from 7 to 8 TeV, we find a remarkable agreement between the 7 and 8 TeV predictions. For example, we present in Fig. 9 the double ratio

$$\frac{1}{\sigma_5^{7 \text{ TeV-LO}}} \frac{d\sigma_5^{7 \text{ TeV-LO}}}{d\eta} \bigg/ \frac{1}{\sigma_5^{8 \text{ TeV-LO}}} \frac{d\sigma_5^{8 \text{ TeV-LO}}}{d\eta}.$$

For simplicity we do not expand the double ratio in α_s . Since the NLO corrections are moderate in size we do not expect a significant change in the prediction—the difference is formally of higher order in α_s . As can be seen in Fig. 9, the normalized rapidity distribution changes by less than 5% when going from 7 to 8 TeV. For the transverse momentum distribution we expect a harder spectrum for a center-of-mass energy of 8 TeV compared to 7 TeV. This is indeed observed in Fig. 10. The fact that for low transverse momenta the ratios are below 1 is an effect of the normalization to the total cross section. For 8 TeV the regions where the inclusive cross section gets significant contributions is extended to larger p_T , leading to a ratio below 1 when

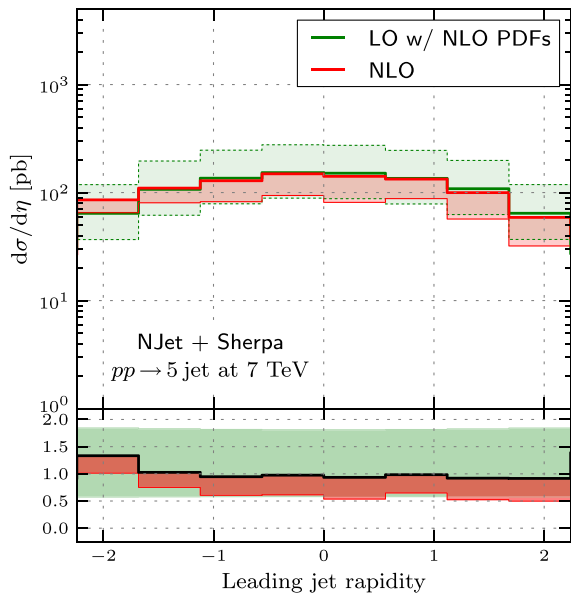


FIG. 8 (color online). The rapidity distribution of the leading jet. Both LO and NLO use the NNPDF2.3 PDF set with $\alpha_s(M_Z) = 0.118$.

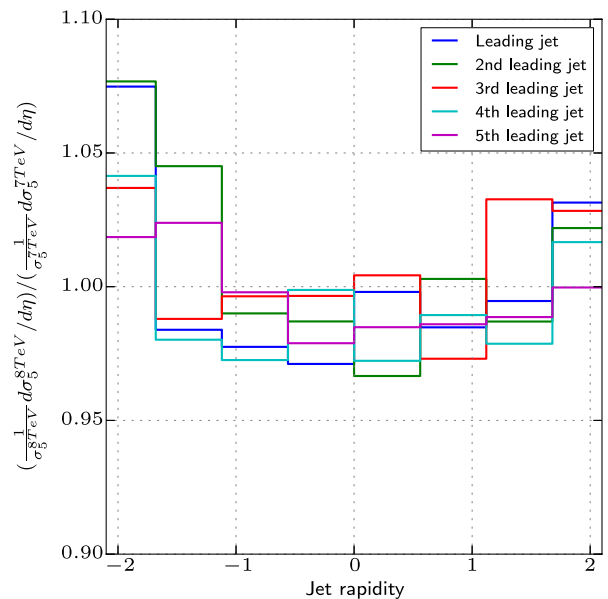


FIG. 9 (color online). Comparison of LO rapidity distributions of the p_T ordered jets for 7 and 8 TeV.

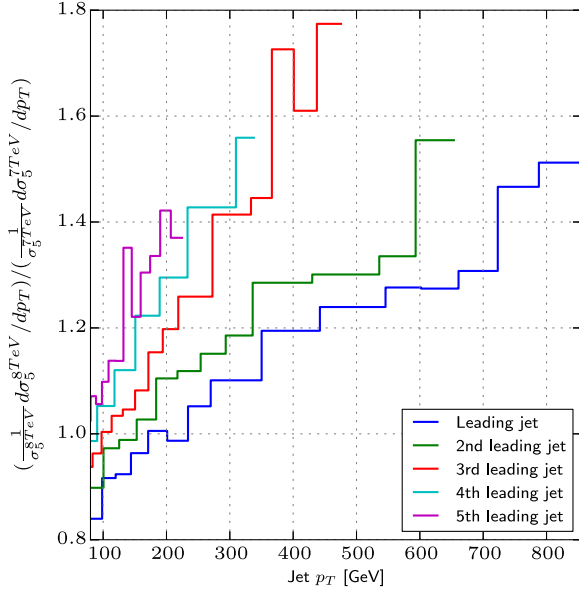


FIG. 10 (color online). Comparison of LO p_T distributions of the p_T ordered jets for 7 and 8 TeV.

comparing with the 7 TeV case. Using data for jet production may provide useful input to constrain PDFs. In this context it is very interesting to study the decomposition of the jet rates with respect to individual partonic channels not only for inclusive quantities but for differential distributions as well. In Fig. 11 the decomposition of the rapidity distribution of the leading jet is shown. As in the inclusive case we restrict the discussion

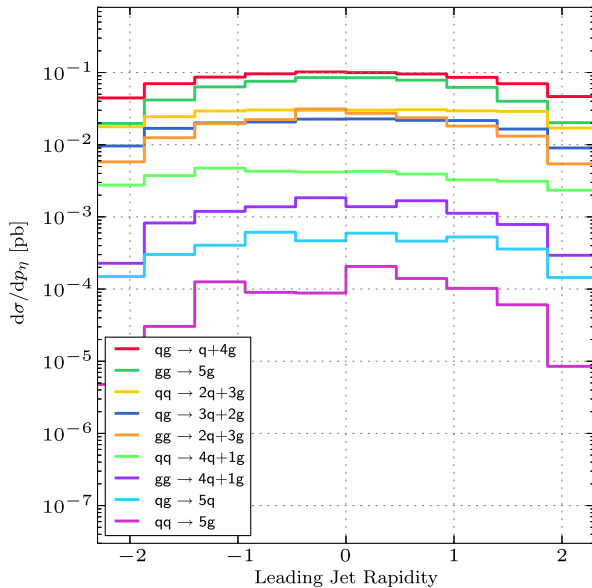


FIG. 11 (color online). Contribution of the different partonic channels to the leading jet rapidity distribution.

to leading order. Evidently we find again that the $qg \rightarrow q + 4g$ channel is the most important channel, followed by the pure gluonic channel. Since the rapidity distribution is only mildly affected by the partonic center-of-mass energy we do not expect a strong rapidity dependence of the composition. Indeed, as can be seen from Fig. 11 the decomposition shows only a weak dependence on the rapidity. This information can be used to define control samples when using jet data to constrain the parton luminosities. In Fig. 12 the analogous results for the transverse momentum distribution are presented. Unlike the rapidity distribution, a significant dependence of the decomposition on the transverse momentum is visible. While at small transverse momentum the $gg \rightarrow 5g$ dominates over $qq \rightarrow 2q + 3g$, the situation changes at about 300 GeV and the $qq \rightarrow 2q + 3g$ becomes more important than $gg \rightarrow 5g$. This behavior is a direct consequence of the fact that at high partonic center-of-mass energies the quark luminosity $\mathcal{L}_{q\bar{q}}$ dominates over the gluon flux \mathcal{L}_{gg} . A similar pattern—although less pronounced—can also be observed in the $qq \rightarrow 5g$ and $gg \rightarrow 4q + 1g$ channels. A cut in the transverse momentum can thus be used to change the mixture of the individual partonic channels and to provide additional information on specific parton luminosities. From the above discussion we expect that different PDF sets should give very similar results for the rapidity distribution since each bin is rather inclusive with respect to the partonic center-of-mass energies where the luminosities are sampled. On the other hand, if any difference is observed when using PDF sets from different groups it will most likely show up in the transverse momentum distribution. In Fig. 13 the rapidity

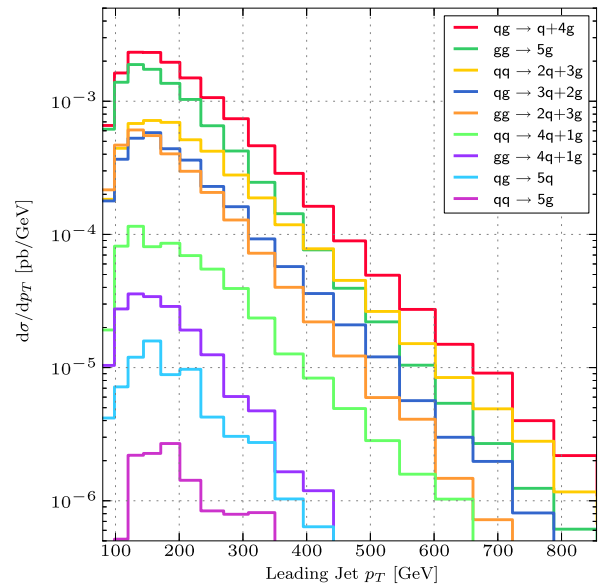


FIG. 12 (color online). Contribution of the different partonic channels to the leading jet p_T distribution.

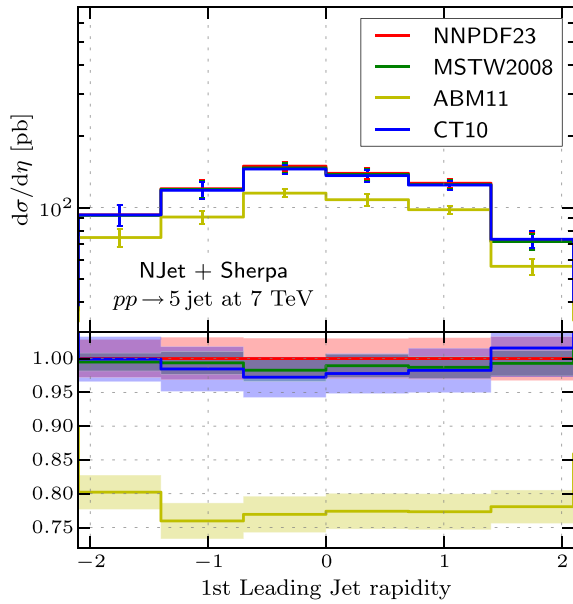


FIG. 13 (color online). Comparison of different PDF sets on the rapidity distributions. All sets use $\alpha_s(M_Z) = 0.118$. The lower plot shows the ratio of the various PDF sets with respect to NNPDF2.3. Error bars in the upper plot are MC errors while shaded areas in the lower plot are PDF uncertainties.

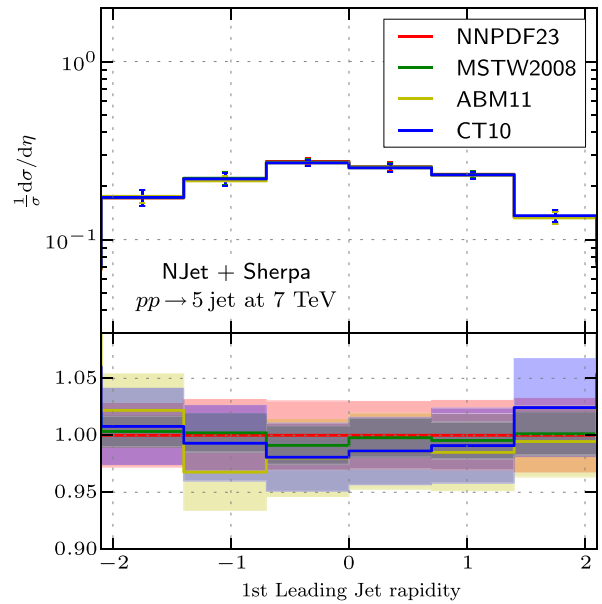


FIG. 14 (color online). Comparison of different PDF sets on the rapidity distributions normalized to the total cross section. The lower plot shows the ratio of the various PDF sets with respect to NNPDF2.3. Error bars in the upper plot are MC errors while shaded areas in the lower plot are PDF uncertainties.

distribution is shown using four different PDF sets. The PDF sets NNPDF2.3, CT10, and MSTW2008 lead to very similar results. A major difference is observed when comparing the aforementioned PDF sets with ABM11. ABM11 leads to a reduction of about 20% with respect to NNPDF2.3, CT10, and MSTW2008. However, one can see that the shape for the distribution predicted by ABM11 agrees well with the other PDF sets. In Figs. 14 and 15 we show results for the normalized distributions. For the rapidity distribution the four different PDF sets agree well within $\pm 5\%$. The rapidity distributions of the subleading jets show a similar behavior. In Fig. 15 the transverse momentum distribution is studied for different PDF sets. As expected, one can observe a richer structure at large transverse momentum. While minor differences are visible between ABM11, MSTW08, and NNPDF, they still give rather similar results at large p_T at the level of 10%–15%. However, the CT10 PDF set leads to significantly larger results at large p_T . In the highest- p_T bin the normalized cross section is enhanced by about 20%–30% compared to ABM11, MSTW08, and NNPDF. Unfortunately it is not easy to distinguish the different predictions experimentally since the cross section for this bin is reduced by several orders of magnitude. A significant amount of data is thus required to achieve the required statistical sensitivity.

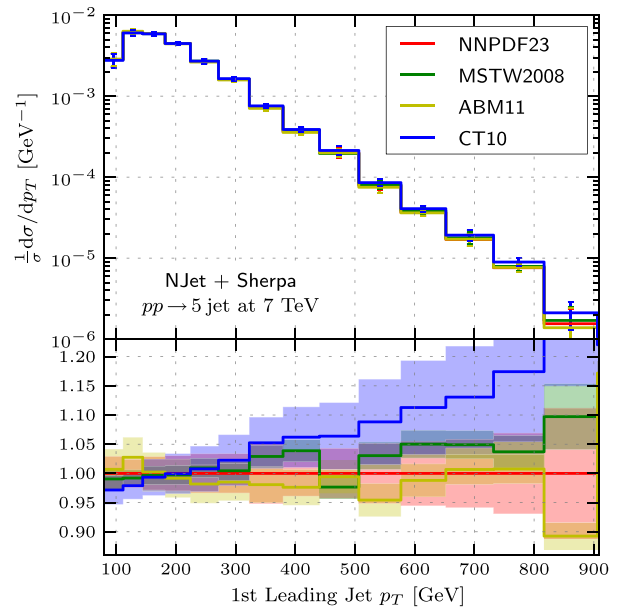


FIG. 15 (color online). Comparison of different PDF sets on the p_T distributions normalized to the total cross section. The lower plot shows the ratio of the various PDF sets with respect to NNPDF2.3. Error bars in the upper plot are MC errors while shaded areas in the lower plot are PDF uncertainties.

IV. CONCLUSIONS

In this article we have presented the first results for five-jet production at NLO accuracy in QCD. We found moderate corrections at NLO with respect to a leading-order computation using NLO PDFs. Typically, corrections of the order of 10% are observed. Identifying the renormalization and factorization scales and using the total transverse momentum \hat{H}_T as a dynamical scale leads to a flat K factor for the differential distributions. We have compared theoretical predictions for inclusive jet cross sections and jet rates with data from ATLAS. With the exception of quantities affected by the two-jet rate we find good agreement between theory and data. As a major uncertainty of the theoretical predictions we have investigated the impact of using different PDF sets. While good agreement is seen between different sets for rather inclusive quantities and distributions that are not sensitive to a specific partonic center-of-mass energy (in the case of distributions this requires one to study normalized predictions), significant differences are observed in the transverse momentum distribution of the leading jet at large momentum.

The analysis of the $(n+1)/n$ jet ratios shows that the 4/3 and 5/4 predictions appear to be perturbatively more stable than the 3/2 predictions with a modest correction at NLO. This indicates that these quantities are good candidates for future extractions of α_s from the LHC data, where reliable fixed-order predictions are mandatory. We hope the results presented here will be useful for these and other analyses in the future.

ACKNOWLEDGMENTS

This work is supported by the Helmholtz Gemeinschaft under contract HA-101 (Alliance Physics at the Terascale), by the German Research Foundation (DFG) through the trans-regional collaborative research center ‘‘Computational Particle Physics’’ (SFB-TR9) and by the European Commission through Contract No. PITN-GA-2010-264564 (LHCPhenoNet). We would also like to thank the DESY Zeuthen theory group for providing computer resources.

APPENDIX A: NUMERICAL ACCURACY OF THE VIRTUAL CORRECTIONS

The details of the numerical evaluation of the virtual amplitudes included in this appendix are highly

TABLE IV. Average accuracy and evaluation speeds achieved during integration of the virtual amplitudes. The abbreviations are as follows: quadruple precision (QP); quadruple precision with scaling test (two evaluations) (QP2); octuple precision (OP).

Virtual part	Time per event	QP	QP2	OP
leading	17 s	2%	0.5%	0.01%
subleading	112 s	2.5%	1%	0.05%

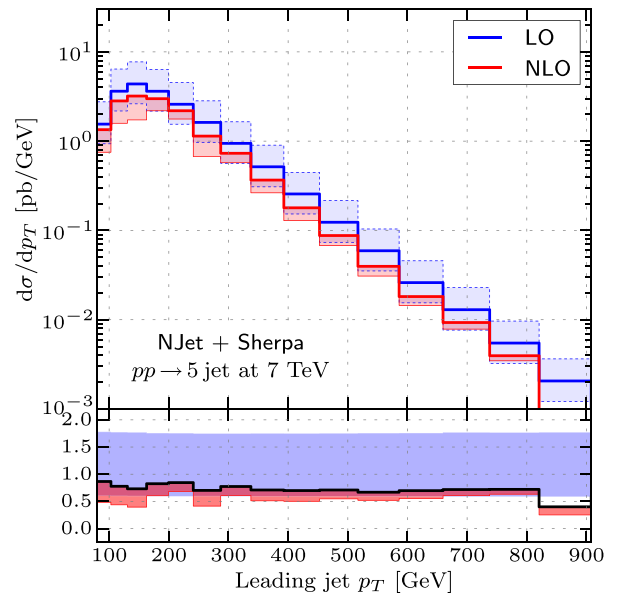


FIG. 16 (color online). p_T distribution of the leading jet. LO uses NNPDF2.1 with $\alpha_s(M_Z) = 0.119$, while NLO uses NNPDF2.3 $\alpha_s(M_Z) = 0.118$.

dependent on the system architecture and integration parameters. In our calculation a large cluster with a wide range of different CPUs has been used and so the information above should be considered only as a guide. We include it here since the results may be of interest to experts in the field.

The virtual matrix elements needed for the computation are complicated and it is important to keep a close eye on numerical stability. In NJET this is done

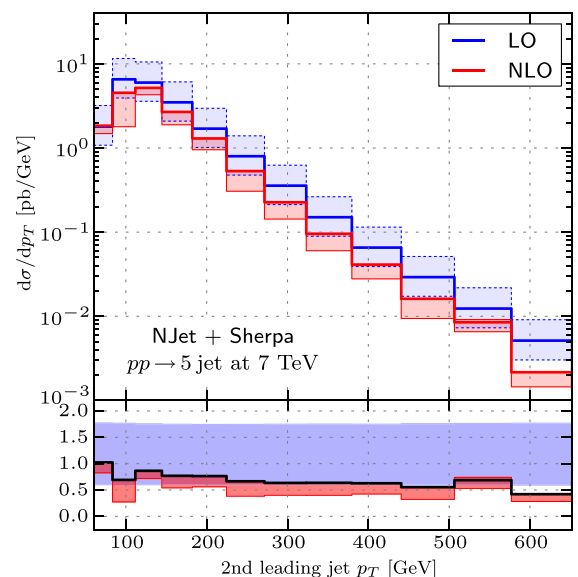


FIG. 17 (color online). p_T distribution of the second leading jet.

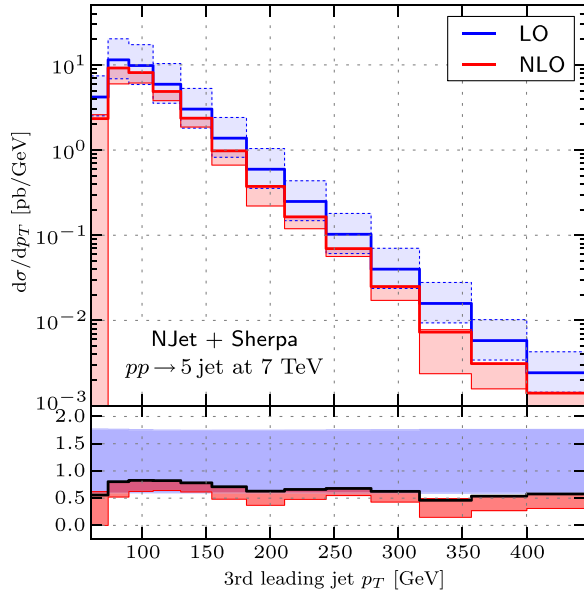


FIG. 18 (color online). p_T distribution of the third leading jet.

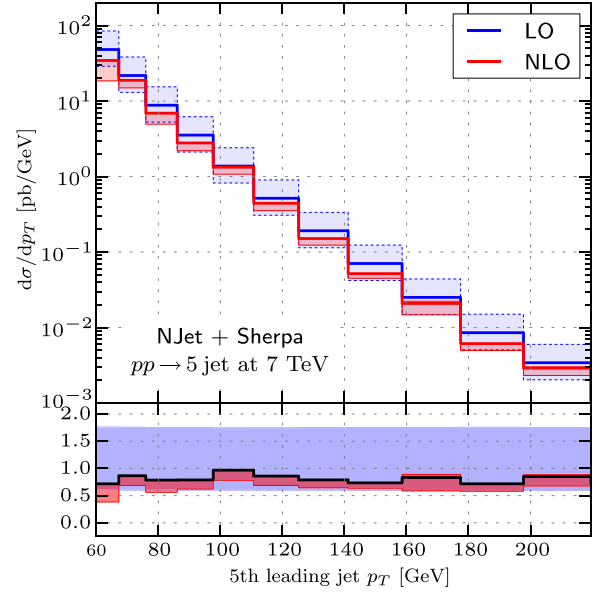


FIG. 20 (color online). p_T distribution of the fifth leading jet.

using the scaling test [11] which evaluates each amplitude twice per phase-space point to obtain a reliable estimate of the numerical accuracy. If fewer than five digits are reliable the point is reevaluated using quadruple precision via the QD library [54]. If one or no digits are considered reliable in the scaling test it is repeated in quadruple precision. If the quadruple precision test fails we can resort to octuple precision; however, in practice this happens so rarely

that it has no effect on the final result. For the present implementation of NJET we improve the computational cost of the virtual cross section by integrating leading color and subleading color parts separately. The leading approximation (which includes desymmetrized sums for processes with more than two final-state gluons) gives about 90 percent of the total virtual contribution, which is around 50 percent of the total cross section. On average, leading color events were

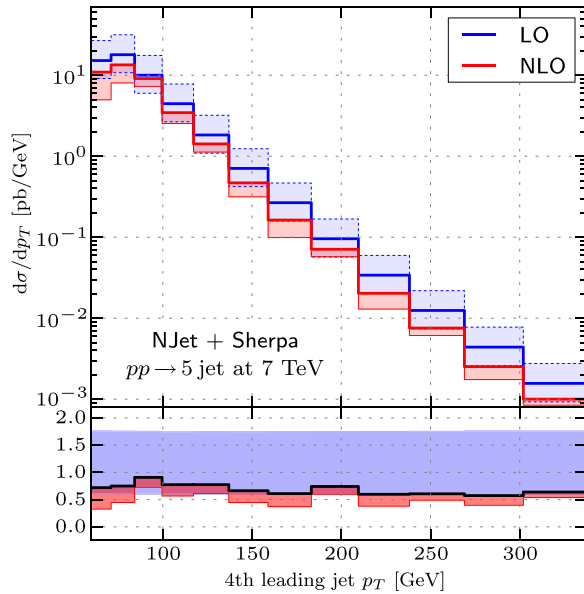


FIG. 19 (color online). p_T distribution of the fourth leading jet.

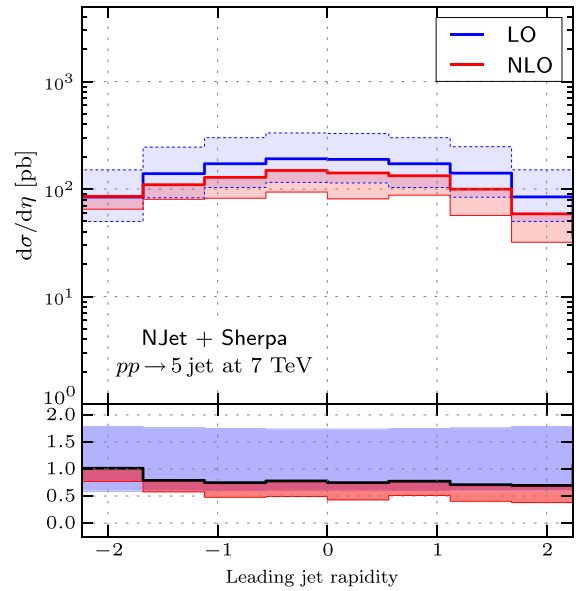


FIG. 21 (color online). η distribution of the leading jet. LO uses NNPDF2.1 with $\alpha_s(M_Z) = 0.119$, while NLO uses NNPDF2.3 $\alpha_s(M_Z) = 0.118$.

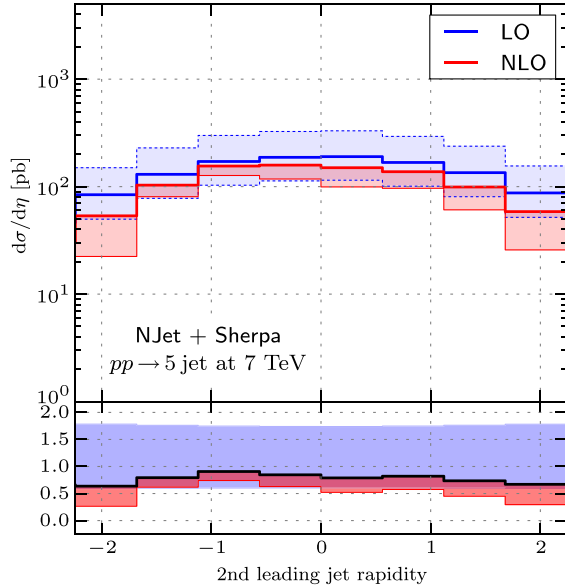


FIG. 22 (color online). η distribution of the second leading jet.

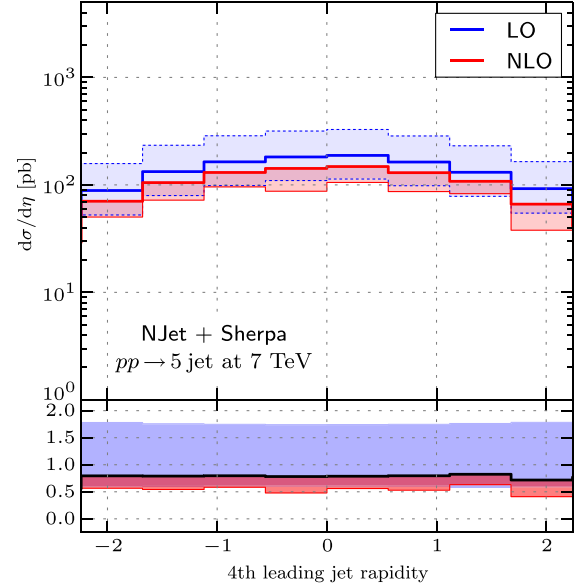


FIG. 24 (color online). η distribution of the fourth leading jet.

generated at 17 seconds per event and subleading color events at just under 2 minutes per event. We found that roughly 2 percent of points required reevaluation using extended floating point precision, with 0.5 percent requiring two evaluations in quadruple precision. Approximately 0.01 percent of points failed the quadruple precision test. Table IV shows a summary of these results.

APPENDIX B: DIFFERENTIAL DISTRIBUTIONS FOR SUBLEADING JETS

In this appendix we present all rapidity and p_T distributions for jets ordered in p_T shown in Figs. (16–25). A complete set of histograms and plots for $\sqrt{s} = 7$ and 8 TeV can be obtained from <https://bitbucket.org/njet/njet/wiki/Results/Physics>.

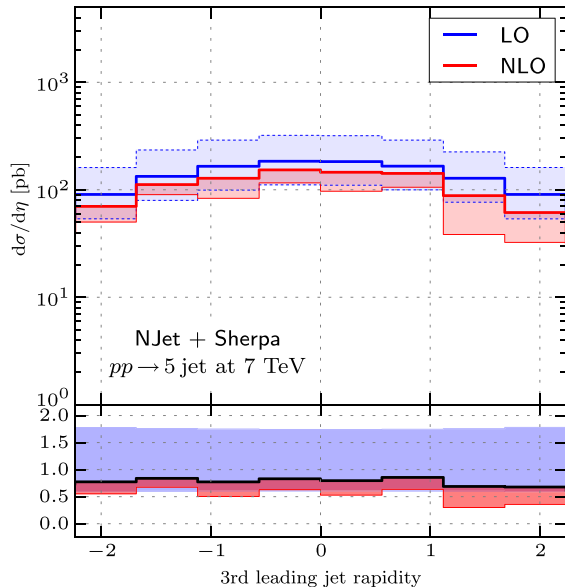


FIG. 23 (color online). η distribution of the third leading jet.

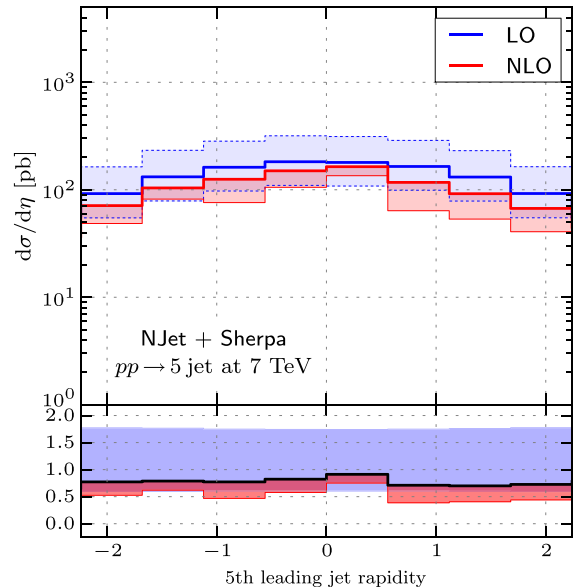


FIG. 25 (color online). η distribution of the fifth leading jet.

TABLE V. Numerical values for the histograms in Fig. 7.

p_{T_1} (GeV)	LO (pb)	NLO (pb)
80.0–98.4	21.4 (0.8)	20.6 (6.3)
98.4–119.7	56.1 (1.3)	51.0 (7.7)
119.7–143.9	86.4 (1.4)	76.4 (7.5)
143.9–171.0	92.1 (1.1)	94.9 (5.4)
171.0–201.1	82.3 (1.1)	81.9 (4.1)
201.1–234.0	66.8 (1.1)	73.7 (4.4)
234.0–269.8	49.7 (0.7)	48.2 (3.5)
269.8–308.5	35.1 (0.4)	38.8 (2.7)
308.5–350.2	22.7 (0.3)	23.8 (1.4)
350.2–394.7	14.2 (0.2)	13.5 (1.1)
394.7–442.2	8.6 (0.2)	8.1 (0.7)
442.2–492.5	4.96 (0.10)	6.4 (1.0)
492.5–545.8	2.81 (0.06)	2.7 (0.3)
545.8–602.0	1.58 (0.05)	1.9 (0.1)
602.0–661.1	0.87 (0.03)	1.0 (0.1)
661.1–723.0	0.50 (0.03)	0.5 (0.1)
723.0–787.9	0.25 (0.02)	0.36 (0.04)
787.9–855.7	0.13 (0.01)	0.12 (0.04)
855.7–926.4	0.065 (0.007)	0.05 (0.02)
926.4–1000.0	0.029 (0.005)	0.04 (0.01)

TABLE VI. Numerical values for the histograms in Fig. 8.

η_1 (GeV)	LO (pb)	NLO (pb)
–2.8–(–2.2)	16.5 (1.3)	14.9 (4.5)
–2.2–(–1.7)	36.0 (0.9)	47.9 (6.4)
–1.7–(–1.1)	60.0 (0.9)	61.6 (6.9)
–1.1–(–0.6)	76.1 (0.8)	72.0 (4.3)
–0.6–0.0	85.6 (0.8)	83.5 (4.3)
0.0–0.6	84.6 (0.8)	79.1 (5.4)
0.6–1.1	75.8 (0.8)	74.6 (3.6)
1.1–1.7	60.8 (1.0)	55.9 (3.7)
1.7–2.2	36.0 (0.8)	33.0 (3.8)
2.2–2.8	15.2 (1.1)	21.1 (5.7)

APPENDIX C: NUMERICAL RESULTS FOR DIFFERENTIAL DISTRIBUTIONS

We provide numerical values for the histograms in Figs. 7 and 8 in Tables V and VI for ease of future comparisons.

- [1] S. Badger, B. Biedermann, P. Uwer, and V. Yundin, *Comput. Phys. Commun.* **184**, 1981 (2013).
- [2] W. Giele, E. N. Glover, and D. A. Kosower, *Nucl. Phys.* **B403**, 633 (1993).
- [3] Z. Nagy, *Phys. Rev. Lett.* **88**, 122003 (2002).
- [4] W. B. Kilgore and W. Giele, *Phys. Rev. D* **55**, 7183 (1997).
- [5] Z. Bern., G. Diana, L. J. Dixon, F. Febres Cordero, S. Höche, D. A. Kosower, H. Ita, D. Maître, and K. Ozeren, *Phys. Rev. Lett.* **109**, 042001 (2012).
- [6] S. Badger, B. Biedermann, P. Uwer, and V. Yundin, *Phys. Lett. B* **718**, 965 (2013).
- [7] G. Aad *et al.* (ATLAS Collaboration), *Eur. Phys. J. C* **71**, 1763 (2011).
- [8] S. Alioli, K. Hamilton, P. Nason, C. Oleari, and E. Re, *J. High Energy Phys.* **04** (2011) 081.
- [9] S. Hoeche and M. Schonherr, *Phys. Rev. D* **86**, 094042 (2012).
- [10] A. G.-D. Ridder, T. Gehrmann, E. Glover, and J. Pires, *Phys. Rev. Lett.* **110**, 162003 (2013).
- [11] S. Badger, B. Biedermann, and P. Uwer, *Comput. Phys. Commun.* **182**, 1674 (2011).
- [12] V. Hirschi, R. Frederix, S. Frixione, M. V. Garzelli, F. Maltoni, and R. Pittau, *J. High Energy Phys.* **05** (2011) 044.
- [13] G. Bevilacqua, M. Czakon, M. V. Garzelli, A. van Hameren, A. Kardos, C. G. Papadopoulos, R. Pittau, and M. Worek, *Comput. Phys. Commun.* **184**, 986 (2013).
- [14] G. Cullen, N. Greiner, G. Heinrich, G. Luisoni, P. Mastrolia, G. Ossola, T. Reiter, and F. Tramontano, *Eur. Phys. J. C* **72**, 1889 (2012).
- [15] A. van Hameren, *J. High Energy Phys.* **07** (2009) 088.
- [16] F. Cascioli, P. Maierhöfer, and S. Pozzorini, *Phys. Rev. Lett.* **108**, 111601 (2012).
- [17] S. Becker, D. Goetz, C. Reuschle, C. Schwan, and S. Weinzierl, *Phys. Rev. Lett.* **108**, 032005 (2012).
- [18] S. Actis, A. Denner, L. Hofer, A. Scharf, and S. Uccirati, *J. High Energy Phys.* **04** (2013) 037.
- [19] G. Bevilacqua and M. Worek, *J. High Energy Phys.* **07** (2012) 111.
- [20] Z. Bern, L. J. Dixon, F. Febres Cordero, S. Höche, H. Ita, D. A. Kosower, D. Maître, and K. J. Ozeren, *Phys. Rev. D* **88**, 014025 (2013).
- [21] G. Cullen, H. van Deurzen, N. Greiner, G. Luisoni, P. Mastrolia, E. Mirabella, G. Ossola, T. Peraro, and F. Tramontano, *Phys. Rev. Lett.* **111**, 131801 (2013).
- [22] H. van Deurzen, G. Luisoni, P. Mastrolia, E. Mirabella, G. Ossola, and T. Peraro, *Phys. Rev. Lett.* **111**, 171801 (2013).
- [23] T. Gehrmann, N. Greiner, and G. Heinrich, *Phys. Rev. Lett.* **111**, 222002 (2013).
- [24] J. Alcaraz Maestre *et al.* (SM and NLO Multileg and SM MC Working Groups), arXiv:1203.6803.
- [25] Z. Bern, L. J. Dixon, D. C. Dunbar, and D. A. Kosower, *Nucl. Phys.* **B425**, 217 (1994).
- [26] Z. Bern, L. J. Dixon, D. C. Dunbar, and D. A. Kosower, *Nucl. Phys.* **B435**, 59 (1995).

- [27] E. Gerwick, T. Plehn, S. Schumann, and P. Schichtel, *J. High Energy Phys.* **10** (2012) 162.
- [28] T. Gleisberg, S. Höche, F. Krauss, M. Schönherr, S. Schumann, F. Siegert, and J. Winter, *J. High Energy Phys.* **02** (2009) 007.
- [29] T. Gleisberg and S. Hoeche, *J. High Energy Phys.* **12** (2008) 039.
- [30] T. Gleisberg and F. Krauss, *Eur. Phys. J. C* **53**, 501 (2008).
- [31] S. Catani and M. Seymour, *Phys. Lett. B* **378**, 287 (1996).
- [32] R. Britto, F. Cachazo, and B. Feng, *Nucl. Phys.* **B725**, 275 (2005).
- [33] R. Ellis, W. Giele, and Z. Kunszt, *J. High Energy Phys.* **03** (2008) 003.
- [34] D. Forde, *Phys. Rev. D* **75**, 125019 (2007).
- [35] C. Berger, Z. Bern, L. Dixon, F. Cordero, D. Forde, H. Ita, D. Kosower, and D. Maître, *Phys. Rev. D* **78**, 036003 (2008).
- [36] G. Ossola, C. G. Papadopoulos, and R. Pittau, *Nucl. Phys.* **B763**, 147 (2007).
- [37] R. K. Ellis, Z. Kunszt, K. Melnikov, and G. Zanderighi, *Phys. Rep.* **518**, 141 (2012).
- [38] W. T. Giele, Z. Kunszt, and K. Melnikov, *J. High Energy Phys.* **04** (2008) 049.
- [39] S. Badger, *J. High Energy Phys.* **01** (2009) 049.
- [40] F. A. Berends and W. T. Giele, *Nucl. Phys.* **B306**, 759 (1988).
- [41] G. van Oldenborgh, *Comput. Phys. Commun.* **66**, 1 (1991).
- [42] R. K. Ellis and G. Zanderighi, *J. High Energy Phys.* **02** (2008) 002.
- [43] T. Binoth *et al.*, *Comput. Phys. Commun.* **181**, 1612 (2010).
- [44] S. Alioli *et al.*, [arXiv:1308.3462](https://arxiv.org/abs/1308.3462).
- [45] M. Cacciari, G. P. Salam, and G. Soyez, *Eur. Phys. J. C* **72**, 1896 (2012).
- [46] M. Cacciari, G. P. Salam, and G. Soyez, *J. High Energy Phys.* **04** (2008) 063.
- [47] M. Whalley, D. Bourilkov, and R. Group, [arXiv:hep-ph/0508110](https://arxiv.org/abs/hep-ph/0508110).
- [48] R. D. Ball, V. Bertone, F. Cerutti, L. D. Debbio, S. Forte, A. Guffanti, J. I. Latorre, J. Rojo, and M. Ubiali (NNPDF Collaboration), *Nucl. Phys.* **B855**, 153 (2012).
- [49] R. D. Ball *et al.*, *Nucl. Phys.* **B867**, 244 (2013).
- [50] J. Andersen *et al.* (SM and NLO Multileg Working Group), [arXiv:1003.1241](https://arxiv.org/abs/1003.1241).
- [51] H.-L. Lai, M. Guzzi, J. Huston, Z. Li, P. M. Nadolsky, J. Pumplin, and C.-P. Yuan, *Phys. Rev. D* **82**, 074024 (2010).
- [52] A. Martin, W. Stirling, R. Thorne, and G. Watt, *Eur. Phys. J. C* **63**, 189 (2009).
- [53] S. Alekhin, J. Blumlein, and S. Moch, *Phys. Rev. D* **86**, 054009 (2012).
- [54] Y. Hida, X. S. Li, and D. H. Bailey, <http://crd-legacy.lbl.gov/~dhbailey/mpdist/>.